Defect-Tolerant Nanocomposites through Bio-Inspired Stiffness Modulation

Allison M. Beese, Zhi An, Sourangsu Sarkar, S. Shiva P. Nathamgari, Horacio D. Espinosa, and SonBinh T. Nguyen**

A biologically inspired, multilayer laminate structural design is deployed into nanocomposite films of graphene oxide-poly(methyl methacrylate) (GO-PMMA). The resulting multilayer GO-PMMA films show greatly enhanced mechanical properties compared to pure-graphene-oxide films, with up to 100% increases in stiffness and strength when optimized. Notably, a new morphology is observed at fracture surfaces: whereas pure-graphene-oxide films show clean fracture surfaces consistent with crack initiation and propagation perpendicular to the applied tensile load, the GO-PMMA multilayer laminates show terracing consistent with crack stopping and deflection mechanisms. As a consequence, these macroscopic GO-PMMA films become defect-tolerant and can maintain their tensile strengths as their sample volumes increase. Linear elastic fracture analysis supports these observations by showing that the stiffness modulation introduced by including PMMA layers within a graphene oxide film can act to shield or deflect cracks, thereby delaying failure and allowing the material to access more of its inherent strength. Together, these data clearly demonstrate that desirable defect-tolerant traits of structural biomaterials can indeed be incorporated into graphene- oxide-based nanocomposites.

1. Introduction

Individual carbon nanostructures such as nanotubes, graphene, or graphene oxide have stiffness and strength that far exceed those of any currently used structural material,[1] making them promising building blocks for preparing macroscopic structural composites.[2] However, attempts to form highly stiff nanocomposites[2c,2d,3] from them thus far have only yielded materials that behave mechanically similarly to brittle ceramics and fracture at far lower strengths than the component nanostructures. This can be explained using the classical Weibull analysis,[4] which indicates that the strength of a brittle, defect-limited material depends on the distribution of defects within it, as well as the volume of the tested sample. Defects limit the apparent tensile strength of the material, as they nucleate cracks that rapidly propagate through the entire sample, leading to catastrophic failure. As the sample size increases, the number of defects will increase and there is a higher probability that some defects will be more severe. In turn, the apparent strength will decrease. This relationship is described in Weibull's weakest-link model, which states that two samples of the same material with effective volumes V_{E1} and V_{E2} will have mean or characteristic strengths σ_1 and σ_2 related by the equation:

$$\frac{\sigma_1}{\sigma_2} = \left(\frac{V_{E2}}{V_{E1}}\right)^{1/m} \quad (1)$$

where m is the Wiebull modulus of the material.[4a,4b,5] Therefore, the apparent strength and size-scalability of a composite is best improved by incorporating defect-tolerance-imparting features that can stop or deflect crack propagation and prevent catastrophic failure upon localized failure at a defect.[6]

In designing defect-tolerant carbon-based nanocomposites, we drew inspiration from the spicules of deep sea sponges,[7] whose fracture toughness is attributed to the periodic stiffness variation in its laminate structure of alternating silica and protein layers. Such stiffness variation has been shown theoretically to hinder crack propagation,[8] and demonstrated experimentally to increase toughness of thin films[9] and multilayer laminates.[10] In this manuscript, we report a combined experimental and computational study that demonstrates how a biologically inspired periodic stiffness modulation can alter the failure mechanisms in a multilayer-laminate composite and dramatically increase its tensile strength and defect tolerance.

2. Results and Discussion

2.1. Preparation and Mechanical Properties of Multilayer-Laminate Composite Films

Composite films comprising 10 alternating graphene oxide (GO) and poly(methyl methacrylate) (PMMA) bilayers, where

Dr. A. M. Beese,[+] S. S. P. Nathamgari, Prof. H. D. Espinosa
Department of Mechanical Engineering
Northwestern University
2145 Sheridan Road, Evanston, IL 60208-3113, USA
E-mail: espinosa@northwestern.edu
Z. An, Dr. S. Sarkar, Prof. S. T. Nguyen
Department of Chemistry
Northwestern University
2145 Sheridan Road, Evanston, IL 60208-3113, USA
E-mail: stn@northwestern.edu
[+]Present address: Department of Materials Science and Engineering, Pennsylvania State University, University Park, PA 16802, USA

DOI: 10.1002/adfm.201303503

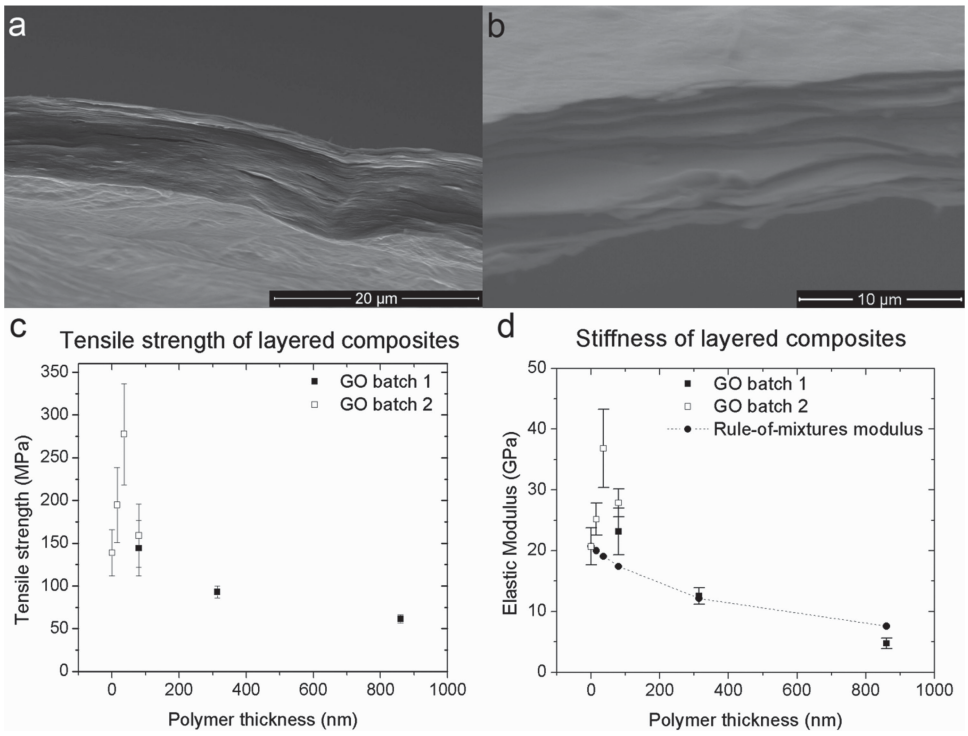

Figure 1. SEM images of the fracture surface of a) a pure-GO film and b) a multilayer laminate. c) Engineering tensile strength and d) stiffness of multilayer laminates as a function of polymer thickness. At least four samples were tested for each polymer thickness; the average stiffness and strength values are shown as data points with the standard deviation indicated by error bars. The modulus described by the rule of mixtures, E_{ROM}, is calculated as $(E_{PMMA}\, t_{PMMA} + E_{GO}\, t_{GO})/(t_{PMMA} + t_{GO})$, where E and t are the modulus and thickness of each component.

the thickness of the GO layers was kept constant at 380 nm while that of the PMMA layers were varied between films, were prepared via spin-assisted layer-by-layer deposition[11] and tested under uniaxial tension. In contrast to the relatively flat fracture planes of pure-GO films, the composite films show terraces that result from crack deflection at the PMMA/GO interfaces (**Figures 1**a,b). Their strength and modulus (Figures 1c,d) increase with decreasing polymer layer thickness (t_{PMMA}), reaching a maximum at t_{PMMA} = 36 nm (average strength = 278 MPa; average modulus = 36.7 GPa), before decreasing to that of the pure-GO control sample (average strength = 139 MPa; average modulus = 20.7 GPa, 10 layers of GO only). Notably, the expected linear rule-of-mixtures composite modulus (E_{ROM}, Figure 1d) is consistently less than the measured modulus for composites with $t_{PMMA} \leq 320$ nm. As the regions of PMMA near graphene oxide can form an interphase with higher modulus than its bulk value,[12] the larger measured modulus in composites with thinner polymer layers can be partially attributed to the increased volume fraction of this interphase. The decrease in measured modulus in the composite where t_{PMMA} = 15 nm may be caused by poor coating of the GO layers, which have a surface roughness of similar height, as determined by ellipsometry.

The aforementioned results suggest that in our system an optimal polymer thickness of ≈40 nm between much thicker GO layers (≈400 nm) provides both high stiffness and high strength. Presumably, the polymer layer can arrest cracks formed by failure at defects in the GO layers, allowing our composites to reach higher strengths than pure-GO films. We note that strong, adhesive interactions between the GO and PMMA layers are unlikely, since delamination at this interface is observed both in the fracture surfaces,[13] which yields the observed terrace structures, as well as during film preparation, where the final step involves the delamination of the bottom GO layer from the sacrificial PMMA layer.

2.2. Computational Analysis

The aforementioned trend of increasing strength with decreasing polymer thickness prompted us to carry out two different, complementary analyses on the composites. The first relies on Weibull statistics to determine the effect of load sharing in the remaining layers when a GO layer is broken. While this approach takes into account the fact that our composites exhibit brittle failure, typically fracturing under 1% of strain and showing scatter in their strength values, it does not yield any information regarding crack propagation. To elucidate whether the incorporation of polymer of a given thickness between GO layers can provide crack-shielding, thereby making the composite more damage-tolerant, we additionally employ linear elastic fracture analysis.

2.2.1. Finite Element Analysis

To computationally model the effect of incorporating soft polymer layers between stiff GO layers on the measured

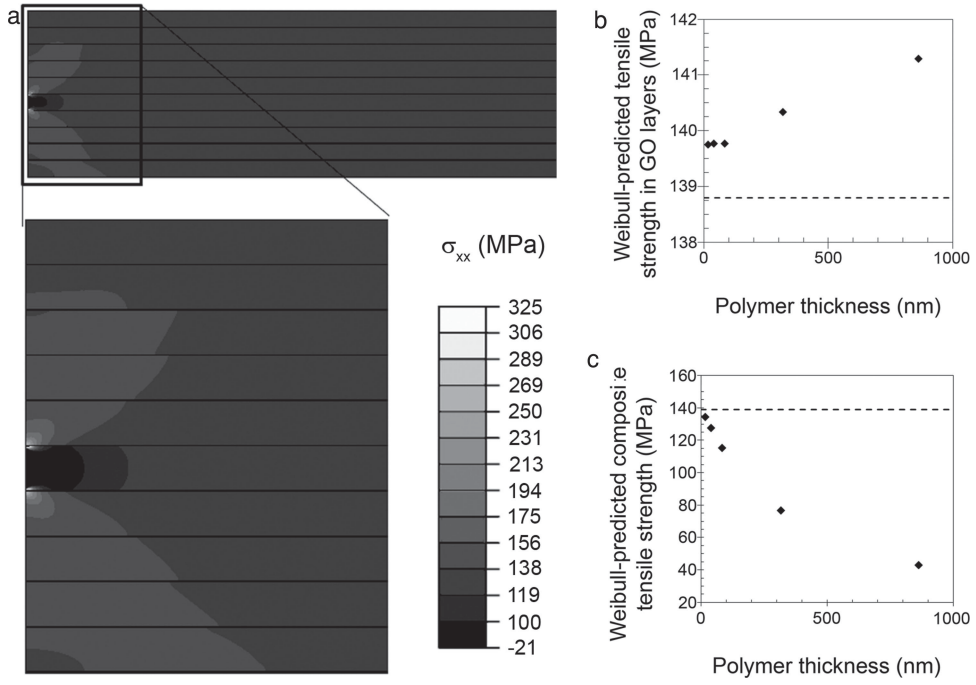

Figure 2. a) Simulated tensile stress contours in a GO-PMMA composite comprising 15-nm-thick polymer layers alternating with 380-nm-thick GO layers. A zoom-in of the high-stress region is also shown. b) Tensile strength of the graphene oxide layers in GO-PMMA composites as predicted by Weibull analysis. c) Composite tensile strength of GO-PMMA composites predicted by Weibull analysis. The dashed horizontal line corresponds to the tensile strength value for the pure-GO control sample made by spin-coating. A color reproduction of this figure is available in the SI as Figure S8.

tensile strength and associated statistics for our composites, we first employ finite element analysis (FEA) to investigate how polymer incorporation affects the load sharing in a composite with a single broken GO layer. Five input geometries, each comprising 10 bilayers of alternating GO and PMMA, were constructed to match the five GO-PMMA composites fabricated and tested in this study. The fifth GO layer is broken to simulate a worst-case defect of a fully broken GO layer. We calculated the load distribution with 1% applied deformation following the fracture of a GO layer (**Figure 2**a; see Figure S6 in the Supporting Information (SI) for remaining contour plots and Section 4.4 for the applied boundary conditions) and the effective volume using Equation (2):[5]

$$V_{\mathrm{E}} = \int_{V} \left(\frac{\sigma_{x}}{\sigma_{\max}}\right)^{m} \mathrm{d}V \tag{2}$$

where dV is the volume of the element being considered; V is the entire volume (unit thickness) of the simulated composite; m is the Weibull modulus, taken here to be 5.6, which is the Weibull modulus for the pure-GO control sample (see Figure S7 in the SI); σ_{x} is the uniaxial tensile stress along the x-direction in the element; and $\sigma_{\max}$ is the reference maximum stress, which is taken as the average strength of the pure-GO control sample (138 MPa).

Applying Equation (2) to the calculated contours of maximum principal stress in each simulated composite geometry reveals that the effective volume increases as the PMMA layer thickness decreases due to more effective distribution of the tensile load to neighboring GO layers, resulting in more GO layers loaded with higher stresses. Assuming that the GO layers bear the entire load, the Weibull model (Equation (1)) then predicts lower strengths for composite samples with thinner polymer layers due to their larger effective volumes, which result in more flaws being sampled (Figure 2b). However, when the polymer thickness is included, the strength of the composite is predicted to increase with decreasing t_{PMMA}, with the pure-GO film having the highest predicted strength (Figure 2c). This is in stark contrast to experimental results, which show strength to actually increase with the addition of thin ($t_{\mathrm{PMMA}} \leq$ 320 nm) PMMA layers. Therefore, the Weibull analysis can at best provide a lower bound for the strength of our GO-PMMA composites; it ignores the enhanced strength by the crack-deflection mechanisms as analyzed below. We note that the increase in effective volume with thinner polymer layers causes the composites to behave more similarly to a monolithic brittle material, resulting in increased scatter in strength for composites with thinner polymer layers compared to those with thicker ones.[14]

2.2.2. Linear Elastic Fracture Analysis

Inspired by the structures of various natural materials such as bone, nacre, and biosilica in deep sea sponges, which have periodically varying moduli, Fratzl and co-workers[8a] carried out a linear elastic fracture analysis of a theoretical model of these materials to determine how the crack-tip driving force changes as a crack propagates through the alternating stiff and soft

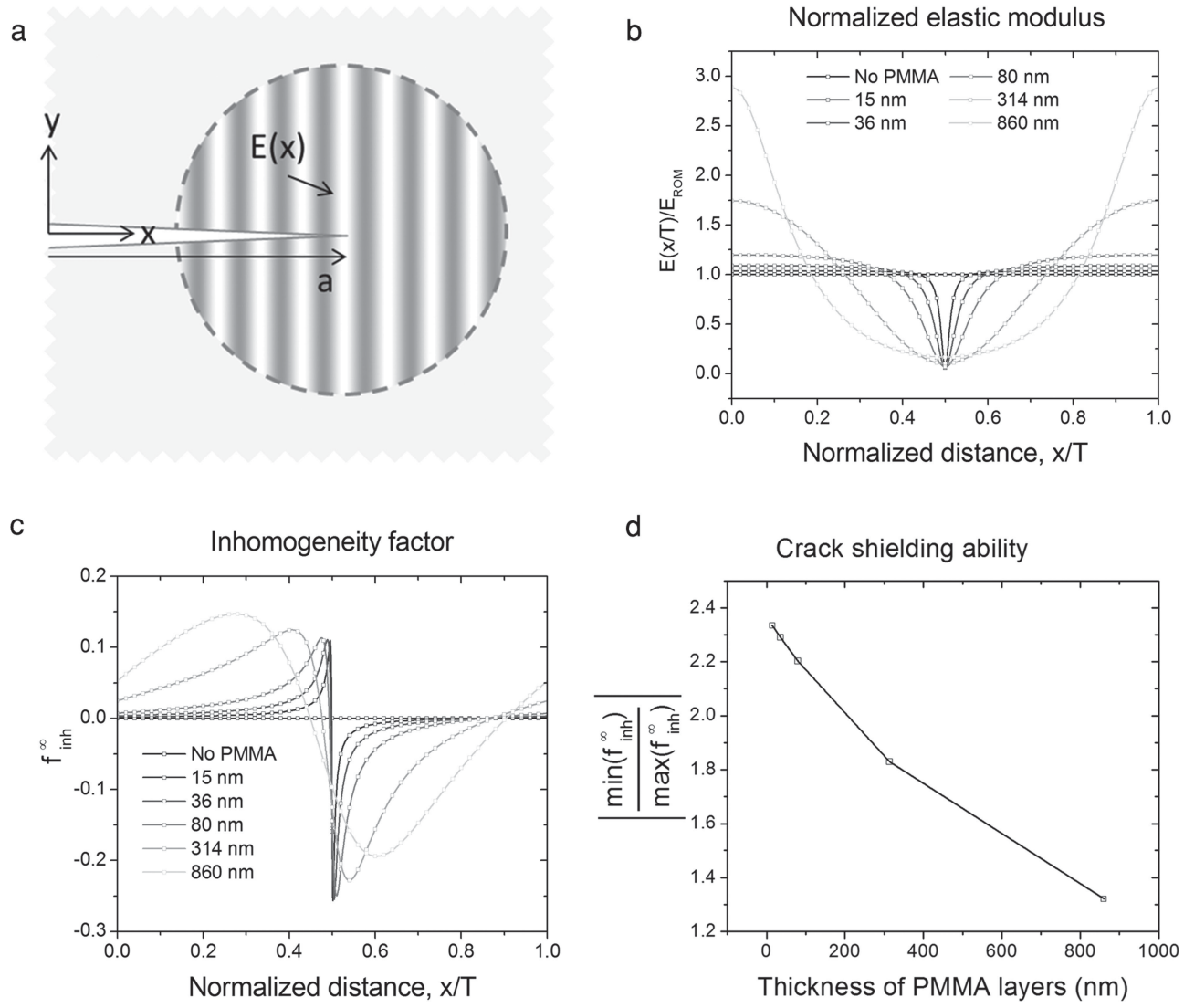

Figure 3. a) A schematic drawing of the propagation of a crack of length *a* through a material with periodically varying elastic modulus along the *x* direction. Figure is adapted from the work by Fratzl and co-workers.[8a] b) The local elastic modulus $E(x/T)$, normalized by the far-field elastic modulus, taken as E_{ROM}, for the five bilayer composites and pure-GO samples studied in this work. c) The inhomogeneity factor f^{∞}_{inh} as a function of the crack length *a* through the unit composite thickness. d) Absolute values of the ratio of the minimum value of f^{∞}_{inh} to its maximum value as a function of polymer thickness. A color reproduction of this figure is available in the SI as Figure S9.

layers in such a material, similar to the ones tested in this study. Because previous fracture mechanics analyses have shown that variations of properties within a material can provide shielding or anti-shielding effects to the crack tip even without incorporating weak interfaces,[15] they hypothesized that the crack-tip driving force can change to hinder or aid crack propagation as a crack advances through regions of varying mechanical properties.

Below, we briefly discuss the analysis that Fratzl and co-workers performed on their model material and relate it to the composites studied here; we refer the reader to the original references[8a,16] for the full analysis. The model material that Fratzl and co-workers analyzed was defined to have unit thickness with an elastic modulus that varies periodically along the *x*-axis (**Figure 3**a).[8a] A crack of length *a* was then introduced, which propagates through the *x*-axis of the model material that has been loaded in tension along the *y*-direction far from the crack. The thermodynamic driving force at the tip of the crack, J_{tip}, is given by:

$$J_{tip} = J_{far}(1 + f_{inh}) \quad (3)$$

where J_{far} is the classical *J*-integral for a path far away from the crack tip and f_{inh} is a local inhomogeneity factor, which quantifies the effect of crack shielding or anti-shielding near the crack-tip that the material inhomogeneity (i.e., its varying modulus) provides. If $f_{inh} < 0$, the inhomogeneity provides crack shielding, meaning that the crack driving force is reduced with respect to that for a homogeneous material. On the other hand, crack anti-shielding results if $f_{inh} > 0$, increasing the

crack driving force comparing to that for a homogeneous material. From Equation (3), it is clear that varying the modulus to achieve $f_{inh} < -1$ can arrest cracks.

For our composites, the spatially varying elastic modulus[8a,16] can be described as:

$$E(x) = \gamma E_0 \left[1 - \frac{\lambda}{(1-\mu/2) + \mu/2 \cdot \cos(2\pi x/T)} \right] \quad (4)$$

with

$$\lambda = 1 \frac{E_{max}}{p_0 E_0} \quad (5)$$

$$\mu = \frac{E_0^2 - E_{max}E_{min}}{E_0[2E_0 - (E_{max} + E_{min})]} \quad (6)$$

$$\gamma = \frac{\sqrt{1-\mu}}{\sqrt{1-\mu-\lambda}} \quad (7)$$

$$p_0 = -\frac{1}{2(1-\nu)}, p_0' = \frac{1-2\nu}{2(1-\nu)} \text{ for plane strain} \quad (8)$$

where E_0 is the far-field modulus, taken as E_{ROM}; E_{max} is the modulus of the stiff material, taken to be the modulus of graphene oxide films (31 GPa,);[2e] E_{min} is the modulus of the soft material, taken to be that of PMMA (1.8 GPa); ν is the Poisson ratio, taken as 0.3[17]; and T is the period over which the modulus varies. To be consistent with the data for GO films that have been reported in the literature, we elect to use an average modulus value of 31 GPa for both the FEA/Weibull and linear elastic crack propagation analyses. We note, however, that the use of a GO modulus of 20.7 GPa, as obtained in this study for spin-coated GO films, will not affect the trends or conclusions made in the FEA or linear elastic crack propagation analyses: the much smaller modulus of the PMMA layer still yields large relative modulus differences between the two components that factor into both the FEA and linear elastic crack propagation analyses.

While a smoothly varying elastic modulus through the thickness of the composite may appear as a poor approximation for our GO-PMMA composites, it is reasonable to assume that there is indeed a gradient through the thickness of the soft PMMA layer, with the polymer in the boundary interphase having a higher modulus than that away from the GO layer.[12a] Thus, the Fratzl analysis[8a] can be used as a qualitative tool to determine whether or not the incorporation of PMMA between the GO layers provides a means to stop or slow crack propagation through the entire composite, thus allowing it to achieve higher strengths than pure-GO films.

The inhomogeneity factor far from the cracks, denoted as f_{inh}^{∞}, can then be obtained as:

$$f_{inh}^{\infty} = p_0 \int_0^T \left(\frac{E_0}{E(a+\xi)} - \frac{E_0}{E(a-\xi)} \right) \frac{d\xi}{\pi\xi} - p_0' \left(\frac{E_0}{E(a)} - \frac{1}{T} \int_0^T \frac{E_0}{E(x)} dx \right) \quad (9)$$

where $\xi = x - a$. Thus, if $f_{inh}^{\infty} -1$, the crack-tip driving force is reduced, and the material inhomogeneity provides crack shielding; and if $f_{inh}^{\infty} 0$, the crack-tip driving force is increased, and the material inhomogeneity provides anti-shielding.

Figure 3b shows the plots of the varying elastic modulus, normalized by E_{ROM}, for the five GO-PMMA composites studied here, along with a control for the pure-GO sample. For these plots, a normalized distance of 0 corresponds to a point halfway through a graphene oxide layer, a distance of 0.5 corresponds to the center of the soft polymer layer, and a distance of 1 corresponds to a point halfway through the next graphene oxide layer (i.e., these plots show the modulus variation over one period T of a bilayer). Figure 3c shows the inhomogeneity factor as a function of the crack length a through the composite. The maximum value for f_{inh}^{∞} corresponds to a location where the crack has entered the soft layer from the stiff layer, meaning at that location, anti-shielding occurs. Conversely, the minimum value of f_{inh}^{∞} corresponds to a location where the crack is about to propagate from the soft layer to the hard layer, giving rise to a strong shielding effect.

To quantify the respective ability for the polymer to provide crack shielding versus anti-shielding in each of the composites studied, we plot the ratio of the absolute values of the minimum f_{inh}^{∞} (crack shielding component) and the maximum f_{inh}^{∞} (crack anti-shielding component) for each of the polymer thicknesses. As shown in Figure 3d, the shielding component increases compared to the anti-shielding component as the polymer thickness decreases, suggesting that very thin polymer layers should increase the crack-shielding capability of the composite, allowing for higher strengths with decreasing polymer thickness. In this manner, thin polymer layers can indeed increase the strength of the composites over that of the pure-GO film, in contrast with predictions from the aforementioned Weibull analysis. Experimentally, however, the strength of the composite may also decrease as smaller amounts of polymer solution are spin-coated onto the rough graphene oxide layers: defects would result where the polymer does not evenly coat the rough graphene oxide surface. Additionally, because PMMA in the boundary layer next to graphene oxide can form an interphase with increased modulus, we hypothesize that the modulus for the very thin 15 nm polymer layer would be higher than that for thicker PMMA layers, reducing the effectiveness of the contrasting moduli to arrest the crack by decreasing the ratio of E_{GO} to E_{PMMA}. Taken together, these two effects may explain why the experimental strengths for our composites reach a maximum when the polymer thickness is ≈40 nm, and decrease for thinner polymer layers.

2.3. Effects of Sample Volume

While we did not perform classical K_{IC} fracture toughness tests in this study due to their experimental incompatibility with our nanocomposite thin-film geometry, the combined Weibull-Fratzl analyses as discussed above can explain well the trends in composite strength with varying sample volume. If inherent toughening mechanisms are not present, the composite will fail as a typical brittle material, limited solely by its flaws. However, if the composite incorporates crack-shielding mechanisms, it is likely to exhibit flaw tolerance (i.e., strength remains approximately constant with varying sample volume).

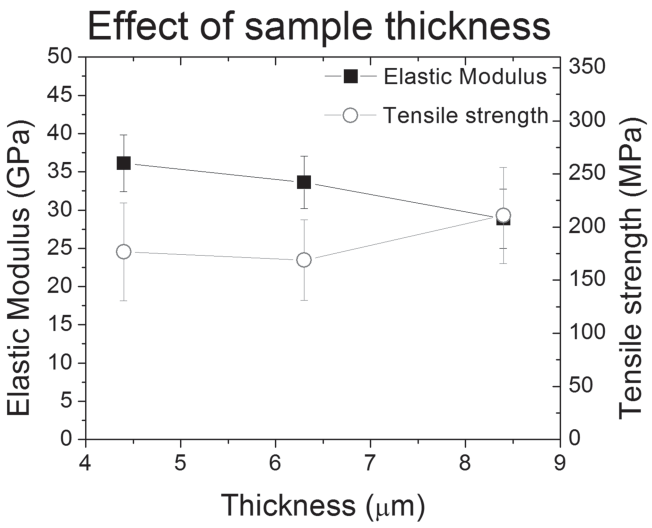

Figure 4. Engineering tensile strength and stiffness of multilayer laminates as a function of sample thickness. We note that these properties were measured using films prepared from a third batch of GO, and should not be quantitatively compared with those of films prepared from other batches (such as those shown in Figure 1). As each batch of GO has different degrees of oxidation and nanosheet dimensions, the films prepared from them also have varying properties. See Section S3 in the SI for additional discussion.

To take advantage of this feature, we increased the overall film thickness, and thus the tested sample volume, by increasing the number of bilayers while keeping gauge length and sample width constant; a constant PMMA thickness of 36 nm was used in all cases.

As shown in **Figure 4**, a detrimental effect on strength was not observed upon increasing the thickness of our layered composite films; rather the strength remains statistically constant. This is in stark contrast to that observed for traditional graphene oxide films where increased thickness results in diminished strength,[2e] as expected from an increase in the probability of finding a dominant flaw. Thus, as the analysis by Fratzl and co-workers suggests, the incorporation of crack-shielding mechanisms through an optimal soft layer between stiff graphene oxide layers can indeed confer defect tolerance to our composites through a toughening mechanism that mitigates crack propagation.

3. Conclusions

In summary, we have shown that the incorporation of thin layers of "soft" PMMA into a "hard" GO film can increase the stiffness and strength of the resulting composites, with an ideal polymer thickness that is determined by the material fabrication method and constituent properties. As shown by linear elastic fracture analysis, such thin layers of polymer are capable of hindering cracks from propagating, yielding a defect-tolerant composite with increased overall strength and improved insensitivity to large sample volumes. Together, these results clearly demonstrate that our multilayer-laminate composites can incorporate the desirable defect-tolerant traits of structural biomaterials. This structure-based approach should be readily compatible with other composite systems and a broad range of nanofillers, including clay tablets, carbon nanotubes, and carbon nanofibers.

4. Experimental Section

4.1. Materials

Graphite powder (SP-1) was used as received from Bay Carbon (Bay City, MI, USA). Sodium nitrate (Sigma-Aldrich, Milwaukee, WI, USA), concentrated sulfuric acid (95–98 wt%, VWR/BDH, Radnor, PA, USA), potassium permanganate (Sigma-Aldrich, Milwaukee, WI, USA), poly(methyl methacrylate) (PMMA, 350K MW, atactic beads, Polysciences, Inc., Warrington, PA, USA), ethanol (absolute, Sigma Aldrich, Milwaukee, WI, USA), and toluene (ACS reagent, >99.5%, Sigma Aldrich, Milwaukee, WI, USA) were obtained from commercial sources and used as received. Hydrogen peroxide (30 wt% in water) was acquired from Sigma-Aldrich and refrigerated when not being used. Ultrapure deionized water (resistivity >18.2 MΩ cm) was obtained from a Milli-Q Biocel system (Millipore, Billerica, MA, USA). Silicon wafers (100 mm diameter, 500 nm thermal oxide, single-side polished) were purchased from Nova Electronic Materials (Flower Mound, TX, USA).

Synthesis of Graphene Oxide: Graphite (5 g) was first oxidized to graphite oxide by a modified Hummer's method,[3a] but with the reaction time extended to 16 h. The resulting graphite oxide was collected by filtration through a fritted glass funnel and washed 5 times with aqueous HCl (≈200 mL of a 3.7 wt% solution), with good mixing during each wash to dissolve remaining inorganic salt and acid impurities. The purified, soft graphite oxide was deacidified by 6 cycles of resuspension in water (≈500 mL), centrifugation (8230 rcf for 5 min in a model 5804R centrifuge (Eppendorf, Westbury, NY, USA)), and decantation. The remaining purified graphite oxide pellets were collected and suspended in ultrapure deionized water, giving an extremely viscous suspension (300 mL total volume). This graphite oxide suspension was then exfoliated into individual graphene oxide nanosheets by bath sonication (6 h, FS60 bath sonicator, Fisher Scientific), diluted with ethanol (300 mL), and sonicated further for 2 h. Any residual unexfoliated graphite oxide was removed by centrifuging at 8230 rcf for 5 min and collecting the supernatant dispersion by pipette.

The collected graphene oxide dispersions were used for film fabrication (see below) right after preparation, as aged solutions (> ≈2 weeks) no longer gave uniform films. We speculate that older graphene oxide solutions would form liquid crystals[18] or slowly decompose,[19] which change the solution rheology and prevent uniform films from being prepared by spin-coating.

The final dispersions contained 15–20 mg mL^{-1} of graphene oxide (GO), with C/O ratios determined by elemental analysis to be 2.11, 1.70, and 1.42 for batches 1,2, and 3, respectively. Accounting for water content (4.9, 2.0, and 5.3 wt%, respectively) results in C/O ratios of 2.38, 1.77, and 1.57, respectively. Qualitative particle sizes were measured by dynamic light scattering (DLS), affording average hydrodynamic diameters of 620, 520, and 1030 nm, respectively, for the three batches of graphene oxide used in this study. (We note that DLS models particles as spheres, which is a poor approximation of graphene oxide nanosheets; however, it can be used to qualitatively compare different samples). We additionally note that films from another batch of graphene oxide with an average hydrodynamic diameter of ≈380 nm were also prepared, but could not be peeled off of the silicon wafers after film fabrication (see below), possibly due to enhanced interaction between the functional groups at the graphene oxide sheet edges and the sacrificial PMMA layer. While graphene oxides with different degrees of oxidation (as evidenced by the varying C/O ratios and XPS and FTIR spectra) can be expected to yield materials with different mechanical

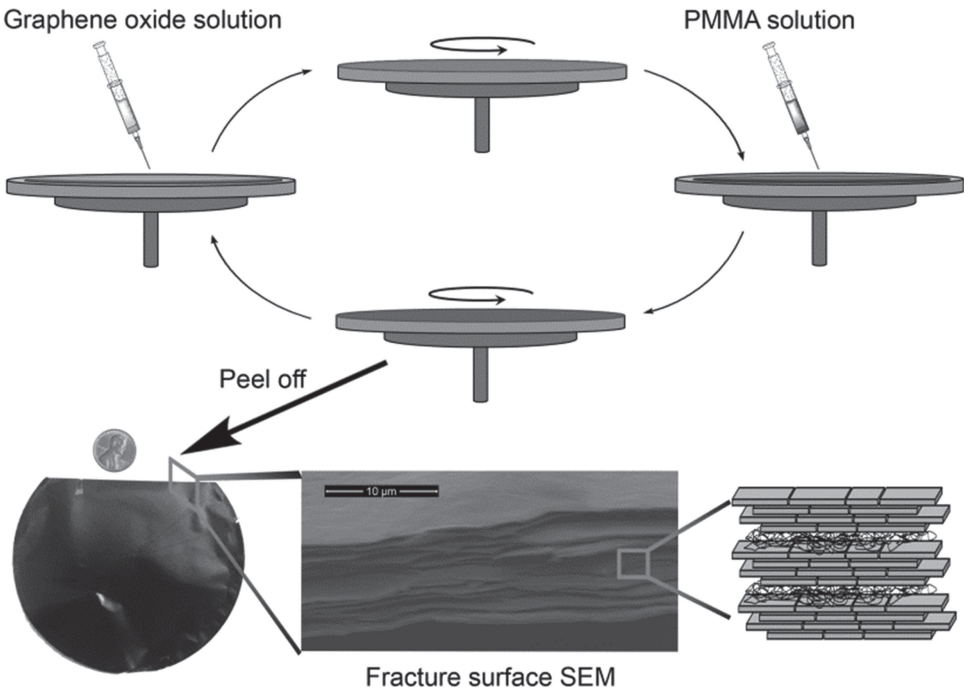

Scheme 1. GO-PMMA multilayer films are prepared via spin-assisted layer-by-layer assembly of (i.e., spin-coating) alternating GO and PMMA layers on a 100 mm silicon wafer, followed by peel off. A US penny is shown next to the peel-off film for size comparison. The resulting films comprise uniform GO layers separated by PMMA layers, which are visible in the SEM image of a fractured surface.

properties, the small ranges of variation in C/O ratios and particle sizes between the batches of graphene oxide used in this study is not expected to result in major changes in mechanical properties. Nevertheless, we have taken care to only make quantitative comparisons of mechanical properties between films prepared using graphene oxide from the same batch. Comparisons of mechanical properties as a function of the level of oxidation and nanosheet size is beyond the scope of this paper, and is not addressed.

Chemical Characterization of Graphene Oxide: Dry films of graphene oxide were produced by drop-casting graphene oxide solution onto silicon wafers, followed by drying at 70 °C. These films were then used for X-ray photoelectron spectroscopy (XPS) (see Figure S1 in the SI). Air-dried films were used for FTIR analysis (see Figure S2 in the SI).

XPS, FTIR, ellipsometry, and DLS were performed in the KECK-II/NUANCE facility at NU using a Thermo Scientific ESCALAB 250Xi (Al Kα radiation, hν = 1486.6 eV) (Thermo Fisher Scientific, West Palm Beach, FL, USA), a Thermo Nicolet Nexus 870, a J.A. Woollam M2000U ellipsometer (J.A. Woollam Co., Lincoln, NE, USA), and a Zetasizer Nano (Malvern Instruments Ltd., Worchester, United Kingdom), respectively. XPS data was analyzed using Thermo Scientific Avantage Data System software, and a Smart background was subtracted prior to peak deconvolution and integration. FTIR data was analyzed using OMNIC software. Ellipsometry was measured at incident angles of 55–75° with 5° steps and wavelengths of 257–1000 nm. Data was analyzed using J.A. Woollam CompleteEASE software using provided material models for PMMA, silicon, and SiO_2, while the optical constants of the graphene oxide layer were modeled using a B-Spline.

CHN elemental analysis by combustion and O elemental analysis by pyrolysis were performed by Micro Analysis, Inc (Wilmington, DE, USA) on films dried at 80 °C under vacuum for 4 h. Water content was measured by Karl Fischer titration using a C20 Compact Karl Fischer Coulometer (Mettler Toledo, Columbus, OH, USA) on films dried at 80 °C under vacuum for 4 h, then sonicated in dry methanol in a sealed vial for 5 min in a bath sonicator.

4.2. Preparation of Multilayer Composite Films and Graphene Oxide Films

Composite films with periodic stiffness variation comprising alternating GO and PMMA layers were prepared by spin-coating onto a silicon wafer (**Scheme 1**) using a model PWM32 spincoater (Headway Research, Inc., Garland, TX, USA). After depositing an initial sacrificial PMMA layer (same thickness as the subsequent PMMA layers), 10 alternating GO and PMMA layers were then deposited (see below for details). The GO layer thickness was kept constant at 380 nm, a value that we found to afford films with good quality and thickness while keeping the fabrication time and material loading manageable. The polymer layer thickness was varied between different films. Following deposition of the final PMMA layer, the resulting film was additionally dried overnight in open air (or in a vacuum dessicator when the ambient humidity is high) then peeled off the substrate (see below for details), leaving behind the initial sacrificial PMMA layer. The final thicknesses of the collected dried films were determined by SEM, and found to closely match the expected thicknesses based on ellipsometry measurements of individual layers.

Spin-Coating of Graphene Oxide Layers: Silicon wafers were flooded with a water-ethanol solution of graphene oxide (prepared as described above) and spun at 300 rpm for 3 min, during which the film thins and dries; followed by 1000 rpm for 3 min and 3000 rpm for 1 min to complete drying, during which no further material is removed from the film as can be visually observed. The thickness of the deposited graphene oxide layer was measured by ellipsometry and this data is used to adjust the concentration of the graphene oxide batch so that a uniform thicknesses of 380 nm can be achieved after each spin-coating deposition, as described above. (As prepared, the different batches of our graphene oxide all gave layers that are ≈50–100% thicker than 380 nm. Thus, each batch was further diluted with ethanol until the right concentration is achieved).

Table 1. Conditions for the spin-coating of PMMA layers of various thicknesses.

Thickness [nm]	Concentration [wt%]	Speed [rpm]	Acceleration [rpm s^{-1}]
860	10	6000	6000
314	5	2000	500
78	2	4000	2000
36	1	4000	8000
15	0.25	4000	8000

As prepared, the deposited layers of graphene oxide all exhibit a "hump" in the center of the wafer with diameter of ≈1 cm that was ≈10% thicker than the rest of the layer. As such, this section of the composite film was not used for mechanical testing. Small radial striations were observed, presumably caused by the different evaporation rates of water and ethanol in the solvent mixture.[20] This type of defect is unavoidable since graphene oxide is insoluble in longer-chain alcohols that evaporate slower than ethanol, and water-only solutions have too high of a surface tension to afford uniform films at slow spin speeds. Because the thickness variation introduced by these striations is within 5%, as measured by ellipsometry with roughness fitting, they were initially expected to have minimum effect on measured mechanical properties. However, as shown in our results, such variation can give a lower limit to the optimal thickness of the PMMA layer that results in the best mechanical properties. That is, the deposited PMMA layer has to be thicker than a lower limit of 15 nm to achieve optimal mechanical properties in this study.

Spin-Coating of PMMA Layers: Silicon wafers were flooded with solutions of PMMA in toluene and then spun for 1 min to form uniform films, with thickness controlled by the concentration and spin-coating conditions given in **Table 1**.

Film Removal: The collection of the films from the silicon wafer was accomplished in several stages (see Figures S3 and S4 in the SI). First, a razor blade was run along the edge of the wafer to remove the excess materials that flowed over the edge of the wafer during deposition. Second, the lip of the film was lifted from the wafer by running the razor blade along the entire circumference of the film, which cuts along the bottom sacrificial PMMA layer. Third, the lip of the film was extended further by pulling it up with a pair of tweezers, which separates the bottom GO layer from the sacrificial PMMA layer. The composite film can then be peeled off by hand like a peel-off sticker, leaving behind the initial sacrificial PMMA layer. Sometimes the bottom GO layer does not separate correctly (see middle picture in Figure S3 in the SI), necessitating peeling from a different direction. The remaining sacrificial PMMA layer does not have any graphene oxide on it.

4.3. Mechanical Testing

As water content has been shown to have significant effects in the mechanical performance of GO films,[21] we equilibrated and tested all the films in a humidity-controlled chamber. To quantify the mechanical properties of the composites, the samples were tested under uniaxial tension. Samples were cut into strips (approximately 3.5 mm wide) and loaded in tension using a microtensile testing frame (Fullam, 2000 lbf rated), equipped with a 5 lbf load cell with 0.125 lbf resolution (Honeywell Model 31, Honeywell International, Inc., Columbus, OH, USA), and a linear variable differential transformer with 1 μm displacement resolution (Allison model HS50, Vishay Precision Group, Inc., Birmingham, UK). Each end of the sample was gripped between two flat grips with sandpaper on the gripping faces to reduce slipping during tensile tests. The gauge length for samples was typically 19 mm, and strain rates on the order of 2×10^{-4} s^{-1} were used for testing. A typical load-displacement curve is shown in **Figure 5**. We note that in these tests, there is typically a load plateau region where the composite slips within the flat grips to achieve alignment with the testing frame's tensile axis. Due to the fragility of the composites, and the non-floating grips in the tensile frame, it was not possible to perfectly align the samples initially with no out-of-plane wrinkles. Thus, to calculate the elastic modulus of a sample, the maximum slope of the force-displacement curve was converted to a modulus value by dividing by the force-displacement slope by the initial length and dividing by the sample cross-sectional area. (We additionally note that this method will yield a lower limit for the elastic modulus, since the cross-head displacement will be greater than the sample elongation due to slippage in the grips.) To obtain the strength of the composite, the maximum force value was divided by the cross-sectional area. Thickness measurements were taken after mechanical testing through scanning electron microscope (SEM) imaging using a Nova NanoSEM 600 (FEI Co., Hillsboro, OR, USA). As the thickness varies slightly throughout the composite (±2–8%), an average of at least 20 thickness measurements was taken for each composite.

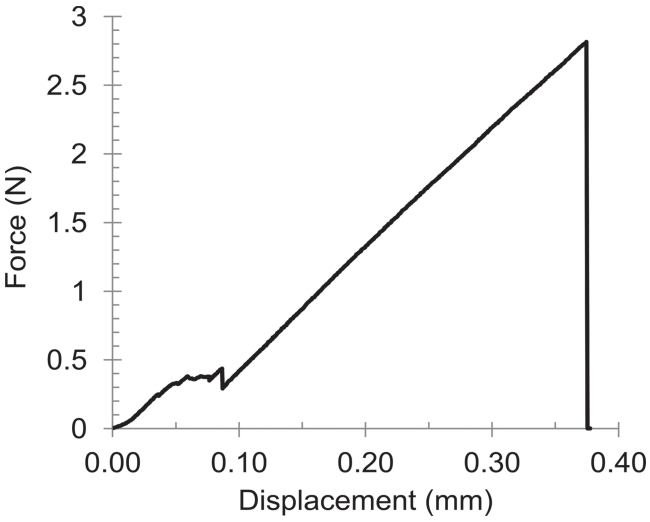

Figure 5. Representative force versus displacement curve up to fracture for graphene oxide/polymer bilayer composites.

4.4. Finite Element Analysis and Weibull Statistical Analysis

Finite element analysis was conducted using Abaqus/Standard version 6.9 software (Dassault Systems, Waltham, MA, USA). Each input geometry comprised of 10 alternating layers of GO and PMMA, yielding a total of 20 layers (Figure S5 in the SI). The GO layer thickness was kept constant at 380 nm, while the PMMA layer thickness was varied to match each experimentally tested sample. The elastic properties of each layer were prescribed as follows: the modulus of PMMA was given as 1.8 GPa with a Poisson ratio of 0.35,[17] and the modulus of the GO layer was given as 31 GPa,[2e] with a Poisson ratio of 0.3 assumed. The length of the simulated region was 15 μm. A unit thickness was used along with generalized plane strain elements (CPE4G).

The following boundary conditions were used: all out-of-plane motions are set to zero; on the left side of the sample, the horizontal (x) displacements of all layers, except for the broken GO layer, are constrained to zero, providing for symmetry about the left vertical axis; and on the right side of the sample, a positive x-displacement corresponding to ≈1% tensile strain is applied to simulate tension applied to the composite material. As the PMMA layers are significantly softer than the GO layers, the vast majority of the applied tensile load is supported by the GO layers regardless of the PMMA thickness. Thus, the applied tensile strain of ≈1% provides for a consistent comparison

of the load transfer for each composite, as the far-field tensile stress in the GO layers in all composite reaches ≈138 MPa. We elect to load the sample to this level as it corresponds to the average tensile stress of the pure-GO control sample in the current study. To eliminate spurious stress concentrations in the GO elements directly neighboring the simulated crack, we define a cutoff stress of 325 MPa, above which the element is considered broken and is not considered in the weighting function. This cutoff stress corresponds to the maximum stress in the GO layers for the strongest composite (for a sample with t_{PMMA} = 36 nm) in the current study.

Supporting Information

Supporting Information is available from the Wiley Online Library or from the author.

Acknowledgements

A.M.B. and Z.A. contributed equally to this work. This research was supported by the ARO (Award # W991NF-09-1-0541). Z.A. is a Ryan Fellow at Northwestern University.

Received: October 12, 2013
Revised: November 20, 2013
Published online: January 29, 2014

[1] a) B. G. Demczyk, Y. M. Wang, J. Cumings, M. Hetman, W. Han, A. Zettl, R. O. Ritchie, *Mater. Sci. Eng. A* **2002**, *334*, 173; b) M.-F. Yu, O. Lourie, M. J. Dyer, K. Moloni, T. F. Kelly, R. S. Ruoff, *Science* **2000**, *287*, 637; c) C. Lee, X. Wei, J. W. Kysar, J. Hone, *Science* **2008**, *321*, 385; d) J. W. Suk, R. D. Piner, J. An, R. S. Ruoff, *ACS Nano* **2010**, *4*, 6557.

[2] a) M. Cano, U. Khan, T. Sainsbury, A. O'Neill, Z. Wang, I. T. McGovern, W. K. Maser, A. M. Benito, J. N. Coleman, *Carbon* **2013**, *52*, 363; b) Q. Cheng, M. Wu, M. Li, L. Jiang, Z. Tang, *Angew. Chem., Int. Ed.* **2013**, *52*, 3750; c) K. Hu, M. K. Gupta, D. D. Kulkarni, V. V. Tsaukruk, *Adv. Mater.* **2013**, *25*, 2301; d) K. Koziol, J. Vilatela, A. Moisala, M. Motta, P. Cunniff, M. Sennett, A. Windle, *Science* **2007**, *318*, 1892; e) D. A. Dikin, S. Stankovich, E. J. Zimney, R. D. Piner, G. H. B. Dommett, G. Evmenenko, S. T. Nguyen, R. S. Ruoff, *Nature* **2007**, *448*, 457; f) E. Munch, M. E. Launey, D. H. Alsem, E. Saiz, A. P. Tomsia, R. O. Ritchie, *Science* **2008**, *322*, 1516.

[3] a) Z. An, O. C. Compton, K. W. Putz, L. C. Brinson, S. T. Nguyen, *Adv. Mater.* **2011**, *23*, 3842; b) X. Zhang, Q. Li, Y. Tu, Y. Li, J. Y. Coulter, L. Zheng, Y. Zhao, Q. Jia, D. E. Peterson, Y. Zhu, *Small* **2007**, *3*, 244; c) W. Lu, M. Zu, J.-H. Byun, B.-S. Kim, T.-W. Chou, *Adv. Mater.* **2012**, *24*, 1805; d) P. Podsiadlo, A. K. Kaushik, E. M. Arruda, A. M. Waas, B. S. Shim, J. Xu, H. Nandivada, B. G. Pumplin, J. Lahann, A. Ramamoorthy, N. A. Kotov, *Science* **2007**, *318*, 80.

[4] a) W. Weibull, *Proc. R. Swed. Inst. Eng. Res.* **1939**, *151*, 1; b) W. Weibull, *J. Appl. Mech.* **1951**, *18*, 293; c) D. G. S. Davies, *Proc. Br. Ceram. Soc.* **1973**, *22*, 429.

[5] G. D. Quinn, *J. Am. Ceram. Soc.* **2003**, *86*, 475.

[6] M. P. Harmer, H. M. Chan, G. A. Miller, *J. Am. Ceram. Soc.* **1992**, *75*, 1715.

[7] a) A. Woesz, J. C. Weaver, M. Kazanci, Y. Dauphin, J. Aizenberg, D. E. Morse, P. Fratzl, *J. Mater. Res.* **2006**, *21*, 2068; b) J. Aizenberg, J. C. Weaver, M. S. Thanawala, V. C. Sundar, D. E. Morse, P. Fratzl, *Science* **2005**, *309*, 275.

[8] a) P. Fratzl, H. S. Gupta, F. D. Fischer, O. Kolednik, *Adv. Mater.* **2007**, *19*, 2657; b) O. Kolednik, J. Predan, F. D. Fischer, P. Fratzl, *Adv. Funct. Mater.* **2011**, *21*, 3634; c) H. Gao*Int. J. Fract.* **2006**, *138*, 101; d) S. Muju, P. M. Anderson, D. A. Mendelsohn, *Acta Mater.* **1998**, *46*, 5385; e) H. Gao, *Int. J. Solids Struct.* **1991**, *27*, 1663.

[9] a) Z. Burghard, L. Zini, V. Srot, P. Bellina, P. A. van Aken, J. Bill, *Nano Lett.* **2009**, *9*, 4103; b) P. C. Wo, X. L. Zhao, P. R. Munroe, Z. F. Zhou, K. Y. Li, D. Habibi, Z. H. Xie, *Acta Mater.* **2013**, *61*, 193; c) P. Podsiadlo, E. M. Arruda, E. Kheng, A. M. Waas, J. Lee, K. Critchley, M. Qin, E. Chuang, A. K. Kaushik, H.-S. Kim, Y. Qi, S.-T. Noh, N. A. Kotov, *ACS Nano* **2009**, *3*, 1564.

[10] a) J. Zechner, O. Kolednik, *J. Mater. Sci.* **2013**, *48*, 5180; b) H.-B. Yao, H.-Y. Fang, Z.-H. Tan, L.-H. Wu, S.-H. Yu, *Angew. Chem., Int. Ed.* **2010**, *49*, 2140.

[11] a) P. A. Chiarelli, M. S. Johal, J. L. Casson, J. B. Roberts, J. M. Robinson, H. L. Wang, *Adv. Mater.* **2001**, *13*, 1167; b) J. Cho, K. Char, J. D. Hong, K. B. Lee, *Adv. Mater.* **2001**, *13*, 1076; c) C. Jiang, S. Markutsya, V. V. Tsukruk, *Adv. Mater.* **2004**, *16*, 157.

[12] a) T. Ramanathan, A. A. Abdala, S. Stankovich, D. A. Dikin, M. Herrera-Alonso, R. D. Piner, D. H. Adamson, H. C. Schniepp, X. Chen, R. S. Ruoff, S. T. Nguyen, I. A. Aksay, R. K. Prud'Homme, L. C. Brinson, *Nat. Nanotechnol.* **2008**, *3*, 327; b) T. Ramanathan, H. Liu, L. C. Brinson, *J. Polym. Sci., Part B: Polym. Phys.* **2005**, *43*, 2269; c) S. Watcharotone, C. D. Wood, R. Friedrich, X. Chen, R. Qiao, K. Putz, L. C. Brinson, *Adv. Eng. Mater.* **2011**, *13*, 400.

[13] K. T. Faber, *Annu. Rev. Mater. Sci.* **1997**, *27*, 499.

[14] The prediction that strength is increased with decreasing t_{PMMA} may also be reached when one considers that the rule of mixtures predicts an increase in modulus with a decrease in PMMA volume fraction and that strength can be estimated as a fraction of the Young modulus (see T.H. Courtney, *Mechanical Behavior of Materials*, 2nd ed., Waveland Press, Inc., Long Grove, IL, USA **2000**) . Nonetheless, the Weibull analysis provides an insight into the increase in effective volume as a source of the observed strength increase.

[15] a) O. Kolednik, *Int. J. Solids Struct.* **2000**, *37*, 781; b) N. K. Simha, F. D. Fischer, O. Kolednik, C. R. Chen, *J. Mech. Phys. Solids* **2003**, *51*, 209; c) B. Ji, H. Gao, *Mater. Sci. Eng. A* **2004**, *366*, 96.

[16] F. D. Fischer, J. Predan, P. Fratzl, O. Kolednik, *Int. J. Fract.* **2012**, *173*, 57.

[17] a) E. T. J. Klompen, Ph.D. Thesis, Eindhoven University of Technology, Eindhoven, Netherlands **2005**; b) D. J. A. Senden, Ph.D. Thesis, Eindhoven University of Technology, Eindhoven, Netherlands **2009**; c) matbase.com, PMMA, http://www.matbase.com/material-categories/natural-and-synthetic-polymers/commodity-polymers/material-properties-of-polymethyl-methacrylate-extruded-acrylic-pmma.html (Accessed August 2013)

[18] a) Z. Xu, C. Gao, *ACS Nano* **2011**, *5*, 2908; b) J. E. Kim, T. H. Han, S. H. Lee, J. Y. Kim, C. W. Ahn, J. M. Yun, S. O. Kim, *Angew. Chem., Int. Ed.* **2011**, *50*, 3043.

[19] a) S. Kim, S. Zhou, Y. Hu, M. Acik, Y. J. Chabal, C. Berger, W. de Heer, A. Bongiorno, E. Riedo, *Nat. Mater.* **2012**, *11*, 544; b) A. M. Dimiev, L. B. Alemany, J. M. Tour, *ACS Nano* **2012**, *7*, 576.

[20] D. P. Birnie, *J. Mater. Res.* **2001**, *16*, 1145.

[21] a) O. C. Compton, S. W. Cranford, K. W. Putz, Z. An, L. C. Brinson, M. J. Buehler, S. T. Nguyen, *ACS Nano* **2011**, *6*, **2008**; b) N. V. Medhekar, A. Ramasubramaniam, R. S. Ruoff, V. B. Shenoy, *ACS Nano* **2010**, *4*, 2300.